Cement and Concrete Composites 115 (2021) 103863

Contents lists available at ScienceDirect

Cement and Concrete Composites

journal homepage: http://www.elsevier.com/locate/cemconcomp

Machine learning to predict properties of fresh and hardened alkali-activated concrete

Eslam Gomaa [a], Taihao Han [b], Mohamed ElGawady [a], Jie Huang [c], Aditya Kumar [b,*]

[a] Department of Civil, Architectural, and Environmental Engineering, Missouri University of Science and Technology, Rolla, MO, 65409, USA
[b] Department of Materials Science and Engineering, Missouri University of Science and Technology, Rolla, MO, 65409, USA
[c] Department of Electrical and Computer Engineering, Missouri University of Science and Technology, Rolla, MO, 65409, USA

ARTICLE INFO

Keywords:
Alkali-activated concrete
Slump flow
Compressive strength
Machine learning
Random forest

ABSTRACT

Alkali-activated concrete (AAC) is widely considered to be a sustainable alternative to Portland cement concrete. However, on account of extensive heterogeneity in composition of the aluminosilicates, coupled with the failure of classical materials science approaches to unravel the underlying composition-property linkages, reliable prediction of AAC's properties has remained infeasible. This paper presents a random forest (RF) model to predict two properties of fly ash-based AACs that are important from compliance standpoint – slump flow; and compressive strength – in relation to physiochemical attributes, curing conditions, and mixing procedures of the concretes. Results show that the RF model – once meticulously trained, and after its hyperparameters are rigorously optimized – is able to produce high fidelity predictions of both properties of new AACs. The model is also used to quantitatively assess the influence of physiochemical attributes and process parameters on the AAC's properties. Outcomes of this work present a pathway to optimization of AACs' properties.

1. Introduction

Portland cement (PC) concrete is the most produced-and-used material for the construction of infrastructure. However, the production of PC – currently at ≈ 4 B tons/year, and growing rapidly at the rate of ≈80 M tons/year [1] – presents considerable energy consumption (≈11 EJ/year [2]) and environmental impact (≈9% of global CO_2 emissions [3]) related challenges. Another challenging aspect of PC concrete infrastructure is its susceptibility to degradation (e.g., corrosion of steel-rebar), which could lead to exorbitant costs of repair/re-construction [4], and, in most ill-fated circumstances, culminate with loss of human lives [5]. There is, thus, burgeoning interest in developing binders that are more sustainable, and yet more durable, than PC binders.

Alkali-activated concrete (AAC) – also called geopolymer concrete – is a promising, sustainable alternative to PC concrete [6,7]. The cementing constituent of AAC (i.e., alkali-activated binder) is prepared by mixing amorphous aluminosilicate materials – such as calcined clays (e.g., metakaolin); or industrial byproducts (e.g., fly ash; and blast furnace slag) – with an alkaline activation solution (often referred to as activator) [8]. Typical activation solutions used for formulation of AAC are aqueous solutions of alkali hydroxides (i.e., NaOH; and KOH) and alkali silicates (i.e., Na_2SiO_3; and K_2SiO_3) [1,9,10]. These highly soluble alkali compounds, when mixed with water, dissolve rapidly and raise the pH of the resultant activation solution. At high pH, the elevated presence of hydroxyl (OH^-) and alkali (Na^+/K^+) ions in the activation solution facilitates dissolution of the solid aluminosilicate precursor (e.g., fly ash; and slag), resulting in the release of aluminate ($Al(OH)_4^-$) and silicate ($H_2SiO_4^{2-}/H_3SiO_4^-$) ions into the solution [9]. Following this, the formation of reaction product occurs via the following sequence of steps: (i) precipitation of aluminosilicate (Al-Si) monomers and oligomers; (ii) hydrolysis and polycondensation of Al-Si oligomers to form a gel network [11–13]; (iii) reorganization of the gel and release of water; and (iv) polymerization of the gel, which enhances its binding properties [1,10,13]. The final reaction product (geopolymer: N-A-S-H and/or C-(N)-A-S-H gels) comprises of $[AlO_4]^{5-}$ and $[SiO_4]^{4-}$ tetrahedra linked by oxygen bridges; the alkali cations are incorporated between successive tetrahedra ensuring valence compensation [10] [–] [13]. Ca-rich and Ca-deficient AAC precursors (e.g., fly ashes) result, predominantly, in the formation of C-(N)-A-S-H [including $C\text{-}(N)_0\text{-}A\text{-}S\text{-}H$ that

* Corresponding author. Department of Materials Science and Engineering, Missouri University of Science and Technology, B49 McNutt Hall, 1400 N Bishop, Rolla, MO, 65409, USA.
E-mail addresses: egomaa@mst.edu (E. Gomaa), thy3b@mst.edu (T. Han), elgawadym@mst.edu (M. ElGawady), jieh@mst.edu (J. Huang), kumarad@mst.edu (A. Kumar).

https://doi.org/10.1016/j.cemconcomp.2020.103863
Received 11 May 2020; Received in revised form 25 October 2020; Accepted 26 October 2020
Available online 4 November 2020

forms in high-Ca systems [8,10,14] and N-A-S-H gels, respectively.

Past studies [9,12,13,15] have shown that – compared to PC concrete – AAC can produce lower CO_2-footprint, higher compressive strength, lower permeability, higher thermal and dimensional stability, and better corrosion-resistance. However, to formulate such performance-optimized AAC, it is important to carefully optimize the composition of its precursors (i.e., aluminosilicate composition; and activator) and mixture design (e.g., liquid-to-solid mass ratio; mixing procedure; and curing temperature). This is because the properties of AACs exhibit significant disparities in relation to precursory chemistry and mixture design [16–18].

Among the predominantly-amorphous, aluminosilicate materials that can be used to formulate AAC, fly ash is the prevalent choice because of its widespread availability and abundance [19,20]. Notwithstanding, fly ash, as a function of lineage of its parent coal and its combustion, features substantial diversity in composition. Based on ASTM C618-15 [21], fly ash can be classified into two classes: class C (calcium-rich) and class F (calcium-deficient). Significant research [22–25] has been devoted to developing correlations between composition of precursors (i.e., amounts of Na_2O/K_2O; CaO; SiO_2; Al_2O_3; and H_2O) and properties (e.g., compressive strength) of AACs; success, however, has been inconsistent. This lack of success can be attributed to the overwhelmingly large compositional degrees of freedom – emerging from significant heterogeneity in fly ashes (in terms of their chemical composition, crystallinity and particle size) and activators (in terms of their chemistries) – which, essentially, have disallowed the advancement of clear, (semi-)empirical rules that govern the fundamental linkage between composition and properties of AACs [7,17]. As such, reliable prediction of composition-dependent properties of AACs, based on Edisonian approaches (i.e., iterative and parametric synthesis-testing-analysis cycles [16,18,26]) or conventional theory-based models, has remained infeasible.

Supervised machine learning (ML) – a tributary of artificial intelligence – is a promising approach, with the potential to overcome the limitations of the Edisonian approach. This is because ML is data-driven, and, therefore, capable of predicting composition-dependent properties of heterogeneous materials (such as AAC), even (and especially) in the absence of an across-the-board theoretical understanding. Not surprisingly, in the past decade or so, ML models have been extensively applied to predict various compliance-relevant properties of traditional PC concretes [27–33]. In the context of AACs, prior studies – albeit very few compared to PC concretes – have also employed ML models to predict compressive strength; selected examples are highlighted here. Dao et al. [26,34] applied artificial neural network, adaptive neuro fuzzy inference, particle swarm optimization-based adaptive network-based fuzzy inference system, and genetic algorithm-based adaptive network-based fuzzy inference system to predict compressive strength of AAC in relation to four compositional descriptors (i.e., fly ash content; Na_2SiO_3 content; NaOH content; and water content). Lahoti et al. [35] employed random forest (RF), Naïve Bayes, and k-nearest neighbor models to predict 7-day compressive strength of AAC; the ML models were trained using a small database comprising of 71 unique data-records. Nguyen et al. [36] used two different deep ML models to predict compressive strength of AACs using 8 inputs consisting of compositional descriptors of the precursors and curing conditions. Prem et al. [37] used several ML models – all premised on nonlinear regression – to predict compressive strength AACs in relation to their compositions and mixture designs.

Prior literature referenced above shows that regression-based ML models are able to predict compressive strength of AAC with reasonable accuracy. Notwithstanding, in these studies, prediction performances of the ML models were arguably not tested exhaustively. This is because databases used to train and test the models had limited volume and limited diversity (i.e., small number of inputs, which entails that variations in fly ash compositions and mixture design were limited). Furthermore, prior studies have focused exclusively on compressive strength, and not attempted to predict slump flow – a quantitative measurement of workability, and an important compliance-relevant property – of AACs using ML models. Lastly, in prior studies, the AAC mixing procedure (i.e., protocols used for mixing AAC components, followed by curing) was not varied; therefore, the prediction performance of ML models in relation to mixing procedure is unknown. Such evaluation is important because mixing procedure – akin to precursor composition – imparts significant influences on properties of AACs [38–40]. As an example, minor alterations in the procedure and duration of mixing could substantially alter fresh- (e.g., rheology) and hardened-state (e.g., compressive strength) properties of AAC [41,42]. Palacios and Puerta [41] showed that increasing the mixing time – from a few minutes to several minutes – results in increment of initial and final setting times, workability, compressive strength, and flexural strength of slag-based AAC. Another study [42] also showed that increasing the mixing time from 1 to 10 min resulted in prolongation of time before the initial and final setting of AACs formulated using class C fly ash. Mixing energy – an important component of the mixing procedure, which is directly proportional to the speed of mixing (measured as revolutions-per-minute, or rpm) – when increased, has been shown to result in enhancement of compressive strength of AACs formulated using class C fly ash [1]. As ML models – in particular those based nonlinear regression – have been shown to reliably predict mechanical properties of cementitious materials [27,28,43], it is imperative to evaluate if they would be able to accurately predict fresh-state properties and mechanical performance of AACs, in which *composition-properties* links are presumably more complex than traditional PC concretes. It is also important to evaluate if nonlinear ML models, that are able to produce predictions with sufficient accuracy, are also able to capitalize on the *composition-properties* links to distinguish the influential compositional (input) parameters from the inconsequential ones [44]. This is important because several commonly-used ML models, such as artificial neural network and support vector machine, function like a "black-boxes" [44], from which it is difficult – if not impossible – to construe or leverage the underlying cause-effect correlations.

The study employs a classification-and-regression trees based random forest (RF) model to predict composition-dependent slump flow and compressive strength of AACs. The model is trained using a high-volume database, consisting of >200 unique data-records linking influential physiochemical properties of the precursors (e.g., chemical composition; and specific surface area) and mixing procedure (e.g., curing conditions) of AACs with their properties (i.e., slump flow; and compressive strength). During training of the RF model, emphasis is given to rigorously optimize the underlying hyper-parameters so as to enhance the model's ultimate prediction performance. Prediction performance of the RF model is then benchmarked – using multiple statistical parameters – against a blind (to the model) test dataset. On the basis of aforesaid benchmarking, it is shown that the RF model is able to produce high fidelity predictions, as well as optimizations, of AACs' properties. This study also places emphasis on leveraging the training of the RF model to quantify the influence of each input parameter on the compressive strength and slump flow of ACCs. This enables the determination of input parameters that are highly influential to AACs properties; and those that are largely inconsequential.

2. Experimental method

AACs were formulated using six different class C fly ashes, water, two different liquidous alkaline activation solutions (activators), sand, and coarse aggregates. Details pertaining to chemical composition of the precursors, mixing procedures, and evaluation of AACs' properties are described in the following subsections.

2.1. Materials

Fly Ash: Six different types of fly ashes, sourced from five different power plants located in Missouri (USA), were used. Chemical

composition of the fly ashes, as determined from X-ray fluorescence spectroscopy (XRF) and protocols described in ASTM D4326-13 [45], are shown in Table 1. As can be seen, all fly ashes used in this study are class C. This classification is based on: (i) ASTM C618-15 classification [21], which states that in class C fly ashes, the summation of SiO_2, Al_2O_3, and Fe_2O_3 contents should be between 50-and-70%; and (ii) ASTM C618-19 classification [46], which states that in class C fly ashes, the CaO content should be >18%. Specific surface area (SSA) of the fly ashes were determined using the N_2-based Brunauer-Emett-Teller (BET) method [47]; results are included in Table 1.

Alkaline Activation Solutions: Two different alkali compounds – sodium silicate (Na_2SiO_3) and sodium hydroxide (NaOH) – were used to prepare alkaline activation solutions. Na_2SiO_3 (liquidous solution), with SiO_2/Na_2O of 2.0, had Na_2O content of 14.7%, SiO_2 content of 29.4%, and H_2O content of 55.9% by mass. NaOH (solid) was AR-grade, with >99% purity. Solid pellets of NaOH were used to prepare liquidous activator solution with Na^+ molarity of 10 M; to this end, at room temperature of 23 ± 2 °C, 314 gm of the NaOH solid pellets were mixed with 686 gm of distilled water until all pellets were fully dissolved. The sodium silicate (SS) to sodium hydroxide (SH) ratio was fixed at 1.0 [N·B.: the mass ratio of SiO_2/Na_2O, commonly referred to as silica modulus (M_s) was fixed at 0.61] for all AACs formulated in this study. The aforesaid ratio was chosen to maintain consistency with our previous study [48], and also on the basis of the guidance that has been provided in prior studies. Past studies have shown that due to the high viscosity of the SS solution, a large SS/SH ratio significantly reduces slump flow and deteriorates workability [7,49]. For both ambient curing and curing at elevated temperatures, the optimal SS/SH has been proposed to be ~1.0; in terms of the silica modulus (M_s or SiO_2/Na_2O), the value would be ~0.61 [48]. When SS/SH is increased from 0.50 (SiO_2/Na_2O = 0.36) to 1.0 (SiO_2/Na_2O = 0.61), compressive strength progressively increases. Conversely, compressive strength reduces when SS/SH is increased beyond 1.0 (i.e., when SiO_2/Na_2O > 0.61). For example, when SS/SH ≈ 2.5 (SiO_2/Na_2O ≈ 1.05), the AAC's pore-solution comprises large amounts of condensed silicate rings but fewer low-order uncondensed silicate monomers (especially at early ages), thus resulting in inhibition of fly ash dissolution [50]. More specifically, the large concentration of soluble silicate rings, generated by the SS, hinders the structure formation of the reaction product (polymeric aluminosilicate structures); which, ultimately, results in diminishment of compressive strength [51,52]. When SS/SH is equivalent to ~1.0 (SiO_2/Na_2O ≈ 0.61), the system is rich with depolymerized lower-order species, such as monomers and dimers [48,51,53]. This accelerates fly ash dissolution: by reducing the precipitation of aluminosilicate gel particles onto fly ash particulate surfaces; and by expediting the initiation of polycondensation of geopolymer gel [50]. Furthermore, SS/SH ≈ 1 (SiO_2/Na_2O ≈ 0.61) provides a good balance between the required hydroxyl ions and alkali species; which results in enhanced dissolution of fly ash, and effective leaching of siliceous and aluminate species from the fly ashes, thus resulting in enhanced polymer precipitation kinetics and higher compressive strength [54].

Aggregates: Dolomite and Missouri river sand, with densities of 2760 kg. m^{-3} and 2600 kg. m^{-3} (measured using ASTM C127-15 [55]), were used as coarse and fine aggregates in this study. The aggregates were stored in closed, dry (low relative humidity) environment prior to using them. Particle size distributions of both coarse and fine aggregates were within acceptable limits prescribed in ASTM C33 [56], respectively. The coarse and fine aggregates have fineness modulus [57] of 2.37 and 6.82, respectively.

Table 1
Oxide composition and specific surface area of fly ashes used in this study.

Oxide composition	Fly Ash-1 (%)	Fly Ash-2 (%)	Fly Ash-3 (%)	Fly Ash-4 (%)	Fly Ash-5 (%)	Fly Ash-6 (%)
SiO_2	36.9	37.9	38.0	42.3	40.4	43.9
Al_2O_3	14.0	17.4	18.7	17.9	17.5	20.1
Fe_2O_3	3.52	3.67	4.86	4.73	4.72	4.96
$SiO_2 + Al_2O_3 + Fe_2O_3$	***54.4***	***59.1***	***61.6***	***64.9***	***62.7***	***69.0***
CaO	37.0	28.8	27.1	25.9	24.1	21.2
MgO	4.80	8.00	7.40	4.74	9.39	4.29
Na_2O	1.62	1.85	1.22	1.58	1.17	2.87
K_2O	0.62	0.39	0.47	0.56	0.48	0.70
TiO_2	0.87	1.17	1.40	1.44	1.40	1.36
P_2O_5	0.70	0.71	0.80	0.89	0.79	0.51
MnO	0.03	0.04	0.02	0.04	0.02	0.05
Ignition loss	0.50	0.82	0.60	0.12	0.62	0.40
BET SSA ($m^2.kg^{-1}$)	2560	3925	2722	1446	2858	2921
Amorphous content (%)	70.5	71.4	NA	74.2	76.7	82.8

2.2. Mixing procedure

202 distinct AAC specimens were formulated by mixing fly ash, liquidous alkali activators, excess water [i.e., additional water (not including the water present in the activator) that was added to achieve the target water/fly ash ratio], and aggregates (coarse and fine). Variations in amounts of the aforesaid ingredients – as used to formulate 202 unique AACs – are described in **Supplementary Information**. The aforesaid variations were explicitly accounted for in the database that was consolidated for training and testing of the ML models [N·B.: details pertaining to formulation of the database can be found in section 4.1]. Since there is no ASTM mixing procedure for AAC, this study focused on developing a mixing procedure that led to homogeneous, workable concrete. Thus, the following eight mixing procedures were investigated in this study. The main differences among the mixing procedures listed below are: (i) the sequence of addition of various components of AAC; and (ii) the duration of mixing at each step of the sequence.

Mixing procedure 1: The mixing procedure consists of the following steps: (1) Coarse and fine aggregates were mixed for 1 min; (2) Fly ash was gradually added to, and then mixed with the aggregates for 1 min; (3) Both liquidous alkali activators (Na_2SiO_3 and NaOH solution) were gradually added to, and then mixed with the solid mixture for 1 min; (4) The excess water was gradually added to the mixture for 1 min; and (5) Once all components of AAC were added, the mixture was mixed for 3 min.

Mixing procedure 2: The first two steps were similar to *mixing procedure 1*. The subsequent steps are as follows: (3) The excess water was gradually added for 1 min; (4) Both alkali activators were gradually added for 1 min; and (5) Once all ingredients of AAC were added, mixing was continued for another 3 min.

Mixing procedure 3: The first two steps were similar to *mixing procedure 1*. The subsequent steps are as follows: (3) The excess water was gradually added to the mixture for 1 min; (4) Sodium hydroxide solution was gradually added for 2 min; (5) Sodium silicate solution was gradually for 1 min; and (6) Once all ingredients were added, mixing was continued for another 3 min.

Mixing procedure 4: The first two steps were similar to *mixing procedure 1*. The subsequent steps are as follows: (3) 75% of the excess water was gradually added for 1 min; (4) Both alkali activators were gradually added for 1 min; (5) The remaining 25% of the excess water was gradually added for 1 min; and (6) Once all ingredients were added, mixing was continued for another 3 min.

Mixing procedure 5: The first two steps were similar to *mixing procedure 1*. The subsequent steps are as follows: (3) 50% of the excess water was gradually added for 1 min; (4) 50% of the alkali activators were gradually added for 1 min; (5) Mixing was continued for two additional minutes; (6) The remaining 50% of the excess water was gradually added for 1 min; (7) The remaining 50% of alkali activators were gradually added for 1 min; and (8) Once all ingredients were added, mixing was continued for another 3 min.

Mixing procedure 6: The mixing procedure consisted of the

following steps: (1) Coarse and fine aggregates were mixed for 1 min; (2) 50% of the excess water was gradually added for 1 min; (3) Fly ash was added and mixed for 1 min; (4) The remaining 50% of excess water was gradually added for 1 min; (5) 50% of the alkali activators were added for 1 min; (6) Mixing was continued for one more minute; (7) 50% of the remaining alkali activators were gradually added for 1 min; and (8) Once all ingredients were added, mixing was continued for another 3 min.

Mixing procedure 7: The first two steps were similar to *mixing procedure 1*. The subsequent steps are as follows: (3) The excess water was gradually added for 1 min; (4) 50% of the alkali activators were gradually added for 1 min; (5) Mixing was continued for one more minute; (6) The remaining 50% of the alkali activators were gradually added for 1 min; and (7) Once all ingredients were added, mixing was continued for another 3 min.

Mixing procedure 8: The first two steps were similar to *mixing procedure 1*. The subsequent steps are as follows: (3) The excess water was gradually added over 1 min; (4) The alkali activators were gradually added for 5 min; (5) Once all ingredients were added, mixing was continued for another 5 min.

2.3. Slump and casting

Workability of each AAC mixture was determined using the slump test, as described in ASTM C143-15 [58]. AACs that had acceptable slump flow were cast in 100 × 200 mm plastic cylinders per ASTM C192-16 [59]. The specimens were placed in two layers, wherein each layer was tamped (compacted with the steel roller) 25 times.

2.4. Curing conditions

After casting the fresh concrete in the cylindrical molds, three different curing regimes were applied to the AACs – oven; ambient; and moist curing (described below). Selected AAC specimens were prepared as per *mixing procedures 1-to-7*, followed by curing in oven and ambient curing regimes; all such specimens were tested (for compressive strength) at the age of 7 days. The remaining AAC specimens were prepared as per *mixing procedure 8*; these specimens were cured in all three curing regimes, and tested at the ages of 1, 7, and 28 days. Sequence of steps followed in each of three curing regimes are described below.

Oven curing: (1) The AAC specimens were rested for 2 h at the ambient temperature of 23 ± 2 °C; (2) The specimens were covered with oven bags, and placed in electrical oven at 70 °C for 24 h; (3) The specimens were taken out of the oven, and then demolded and stored at ambient temperature until the testing age; (4) The specimens made using mixing procedures 1-to-7 were stored in the laboratory without any covering until the testing age; and the specimens made using mixing procedure 8 were stored the laboratory, while being covered with plastic bags, until the testing age.

Ambient curing: (1) The AAC specimens were stored at the ambient temperature of 23 ± 2 °C for 48 h; (2) The specimens were demolded and stored at ambient temperature until the testing age; (3) The specimens made using *mixing procedures 1-to-7* were stored in the laboratory without any covering until the testing age; and the specimens made using *mixing procedure 8* were stored the laboratory, while being covered with plastic bags, until the testing age.

Moist curing: (1) The ACC specimens were stored at the ambient temperature of 23 ± 2 °C for 48 h; (2) The specimens were demolded and stored in a moisture room maintained at ambient temperature and relative humidity of 95 ± 5% until the testing age.

2.5. Compressive strength

Compressive strengths of the AAC specimens were tested per ASTM C39-16 [60]. The reported compressive strengths represent the average of three independent results obtained from as many specimens.

2.6. X-ray diffraction (XRD)

Quantitative XRD analysis (see Table 1) was carried out to: identify the crystalline phases; and to quantify the total amorphous content in the fly ashes (prior to mixing) using Rietveld refinement [N·B.: x-ray structure information for germane phases were sourced from standard databases; and an external standard (G-factor approach) was utilized to quantify the x-ray amorphous phases [61–63]]. Four crystalline compounds were found in all fly ashes: quartz (SiO_2); anatase (TiO_2); periclase (MgO); and a calcium aluminate phase ($Ca_9Al_6O_{18}$) (Fig. 1). In fly ashes with relatively high calcium content, additional crystalline compounds were identified: calcium oxide (CaO); and gehlenite ($Ca_2Al_2SiO_7$). In fly ash-1, that had the highest calcium content among the six fly ashes, hatrurite (Ca_3SiO_5) was also detected. In spite of the presence of different crystalline phases, all fly ashes were found to be dominantly amorphous (i.e., >70%$_{mass}$; see Table 1).

3. Overview of the random forest model

This section presents an overview of the random forest (RF) model used in this study. The overview is deliberately kept succinct as the RF model – and, its underlying algorithms, functions, and parameters – have been described in detail in our previous studies [27,28,33,64].

The RF model – a modification of the classification-and-regression decision trees (CART) model – constructs a large number of uncorrelated, (CART) trees as a committee to produce independent outputs, and ultimately averages them to produce the final output [65]. Each tree within the RF model is partitioned via binary splits into "near-homogeneous" terminal nodes; such partitioning is done in recursive fashion until optimal structure of the tree is achieved. RF leverages the technique of bagging [66,67], which ensures that each tree grows from a randomly-selected group of bootstrap samples, each comprising of the same number of inputs as the entire training dataset. RF also leverages another technique, bootstrapping, which helps reduce the variation (underfitting) and bias (overfitting) among the 100s-to-1000s of trees that are grown in the forest [68]. Another advantage of the RF model is that it allows each tree to grow to its maximum size without any smoothening or pruning whatsoever. This helps maintain diversity among the trees (i.e., output of each tree is truly independent of the output of all other trees), thereby allowing the model to not just capture trends in the dataset but also account for outliers.

The RF model contains two hyper-parameters (i.e., *number of trees in the forest*; and *number of splits in each tree*). Both hyper-parameters were optimized in this study using the 10-fold cross validation (CV) method [28,29,33,69] in conjunction with a grid-search method [70] that is described **in** section 5.0.

4. Training and testing of the random forest model

4.1. Training: establishment of composition-property links

Properties of AAC specimens, as evaluated from experiments described in section 2.0, were collated into two databases: compressive strength database (Table 2); and slump flow database (Table 3). The data from two tables are presented in visualized manner in Figure S1 of **Supplementary Information**. Then, the databases were used for training the RF model, and subsequently for evaluating its prediction performance (i.e., ability to predict compressive strength and slump flow of AACs that were precluded from the training database). The compressive strength database consisted of 180 unique data-records; each data-record represented a unique ACC specimen with 20 inputs and 1 output. The inputs included pertinent physiochemical properties of the AAC: chemical composition of the AAC precursors (i.e., mass fractions of all major oxides present in the fly ash + activator); specific

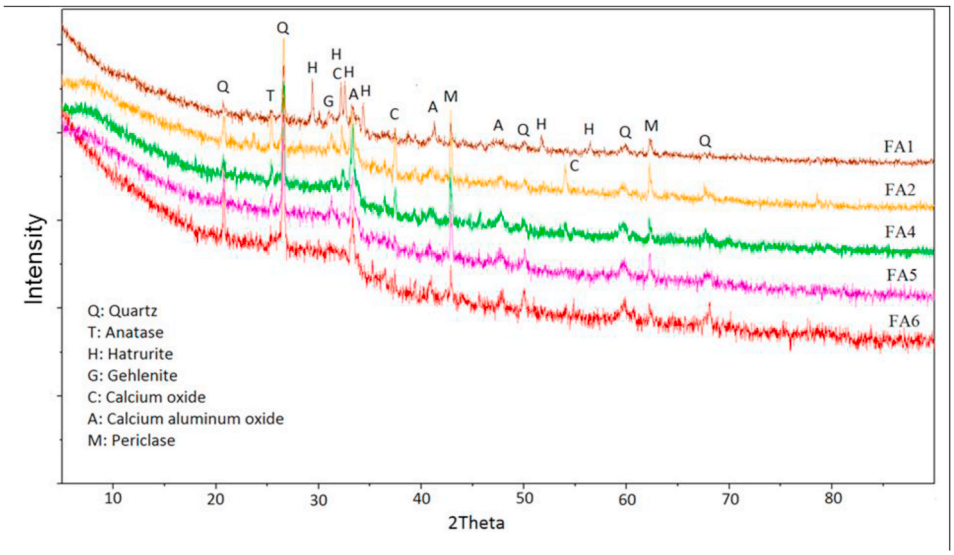

Fig. 1. X-ray diffraction patterns of fly ashes. Crystalline phases present in the fly ashes are indicated.

Table 2
Compressive strength database (volume: 180 distinct data-records), featuring 21 attributes (20 inputs and 1 output).

Attribute	Unit	Min.	Max.	Mean	Std. Dev.
Normalized Coarse Aggregate	Mass fraction	0.0000	0.4248	0.3925	0.0436
Normalized Fine Aggregate	Mass fraction	0.3121	0.6451	0.3370	0.0345
Normalized SiO_2 Content	Mass fraction	0.0655	0.1134	0.0801	0.0078
Normalized Al_2O_3 Content	Mass fraction	0.0259	0.0491	0.0333	0.0039
Normalized Fe_2O_3 Content	Mass fraction	0.0059	0.0112	0.0081	0.0011
Normalized CaO Content	Mass fraction	0.0349	0.0686	0.0459	0.0075
Normalized MgO Content	Mass fraction	0.0079	0.0195	0.0125	0.0034
Normalized Na_2O Content	Mass fraction	0.0093	0.0201	0.0148	0.0021
Normalized K_2O Content	Mass fraction	0.0007	0.0015	0.0010	0.0002
Normalized TiO_2 Content	Mass fraction	0.0016	0.0033	0.0024	0.0003
Normalized P_2O_5 Content	Mass fraction	0.0009	0.0017	0.0013	0.0002
Normalized MnO Content	Mass fraction	0.0000	0.0001	0.0000	0.0000
Normalized Loss on Ignition	Mass fraction	0.0002	0.0021	0.0011	0.0005
Normalized Water Content	Mass fraction	0.0366	0.0923	0.0700	0.0090
SSA of Fly ash	$m^2.\ kg^{-1}$	1446	3925	2611	624
Mixing Procedure	Unitless	1	8	–	–
Curing Regime	Unitless	1	3	–	–
Curing Temperature	°C	23	70	45.19	23.46
Curing Time	Days	1	28	6.15	7.18
Testing Age	Days	1	28	9.58	7.52
Compressive Strength	MPa	1.41	51.45	23.72	10.20

Table 3
Slump flow database (volume: 202 distinct data-records), featuring 17 attributes (16 inputs and 1 output).

Attribute	Unit	Min.	Max.	Mean	Std. Dev.
Normalized Coarse Aggregate	Mass fraction	0.0000	0.4747	0.3945	0.0432
Normalized Fine Aggregate	Mass fraction	0.3121	0.6451	0.3374	0.0330
Normalized SiO_2 Content	Mass fraction	0.0535	0.1134	0.0791	0.0084
Normalized Al_2O_3 Content	Mass fraction	0.0227	0.0491	0.0329	0.0041
Normalized Fe_2O_3 Content	Mass fraction	0.0048	0.0112	0.0080	0.0012
Normalized CaO Content	Mass fraction	0.0313	0.0686	0.0453	0.0075
Normalized MgO Content	Mass fraction	0.0079	0.0204	0.0128	0.0034
Normalized Na_2O Content	Mass fraction	0.0078	0.0201	0.0145	0.0023
Normalized K_2O Content	Mass fraction	0.0006	0.0015	0.0009	0.0002
Normalized TiO_2 Content	Mass fraction	0.0016	0.0033	0.0024	0.0003
Normalized P_2O_5 Content	Mass fraction	0.0009	0.0018	0.0013	0.0002
Normalized MnO Content	Mass fraction	0.0000	0.0001	0.0000	0.0000
Normalized Loss on Ignition	Mass fraction	0.0002	0.0022	0.0011	0.0005
Normalized Water Content	Mass fraction	0.0208	0.0923	0.0696	0.0101
SSA of Fly Ash	$m^2.\ kg^{-1}$	1446	3925	2609	616
Mixing Procedure	Unitless	1	8		
Slump Flow	inch	0	12	5.93	3.07

surface area (SSA) of fly ash ($m^2.\ kg^{-1}$); mixing procedure (unitless; ranging from 1-to-8 as described in section 2.2); curing regime (unitless; ranging from 1-to-3 representing ambient; moist; and oven curing, respectively); curing temperature (°C); curing time (days); and testing age (days). The output parameter included compressive strength (MPa). The slump flow database consisted of 202 unique data-records, wherein each data-record had 16 inputs and 1 output. The inputs consisted of chemical composition of the AAC precursors; SSA of fly ash; and mixing procedure. The output parameter included slump flow (inch). It is pointed out that the two databases have different volumes (i.e., number of data-records) because AAC specimens with very low (<1 inch) or very high (>11 inches) slump could be tested for slump flow but not for compressive strength.

In section 1.0 it was stated that, in AACs, the correlations between physiochemical attributes of the precursors and the resultant properties are highly non-monotonic and nonlinear. The three-dimensional (3D) plots shown in Fig. 2 highlight the complex nature of such correlations.

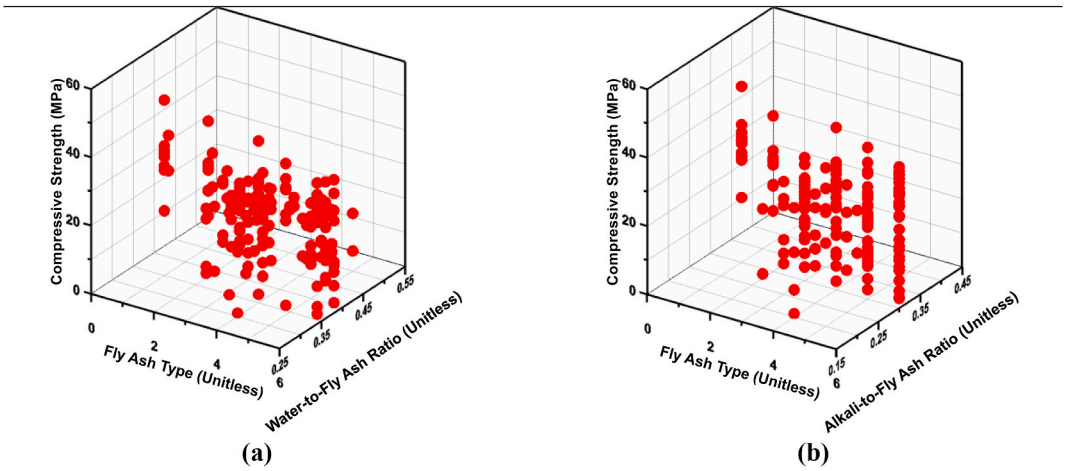

Fig. 2. 3D plots showing compressive strength of AACs (z-axis) in relation to: **(a)** fly ash type and water-to-fly ash mass ratio; and **(b)** fly ash type and alkali activator-to-fly ash mass ratio. In both plots, in addition to the input parameters listed in the x- and y-axes, there are variations in the other 18 other parameters.

Such complexity, nonetheless, is expected because each input parameter – pertaining to either the AAC's precursor chemistry; or the mixture design; or the curing condition – unfailingly casts unique and significant impact on the concrete's properties. When >1 input parameters are concomitantly adjusted – as shown in the x- and y-axes of the plots (Fig. 2) – the cumulative impact on properties is even more complex. Precisely because of such complexities, derivation of empirical, *composition-properties* relationships in AACs is not feasible using simple statistical models; more sophisticated models such as machine learning are needed for such tasks.

4.2. Testing: evaluation of prediction performance

Both experimentally-populated databases (i.e., compressive strength; and slump flow databases, described in section 4.1) were randomly split into two independent (non-overlapping) databases: a training set, containing 75% the parent database's volume, for training the RF model (i.e., optimizing structures of the trees (CARTs), and develop inputs-to-output connections); and testing set, comprising of the remaining 25% of data-records for (blind) testing the model's prediction performance. Justification of the aforementioned 75%-to-25% split in the parent database is provided in several published studies [27,29,31,33,64], and, thus, not reiterated here.

To rigorously assess the prediction performance of the RF model against the two testing datasets, this study used 5 unique statistical parameters: Person correlation coefficient (R); mean absolute percentage error (*MAPE*); coefficient of determination (R^2); root mean squared error (*RMSE*); and mean absolute error (*MAE*). Mathematical formulations for each of these parameters can be found elsewhere [27,33,64].

5. Results and discussion

5.1. Prediction and optimization of AAC's properties

As described in section 4.0, the RF model was trained using 75% (randomly selected) of both databases: compressive strength database and slump flow database. Thereafter, prediction performance of the trained RF model was evaluated against the testing sets of the two databases. To maximize the prediction performance of the RF model – or any other decision trees-based model for that matter – it is important to ascertain that: inputs-output correlations are properly established; outliers are accounted for; and variance and bias among trees of the model are kept as low as possible. To accomplish these objectives, the two hyper-parameters of the RF model (i.e., *number of trees in the forest*; and *number of leaves per tree*) ought to be rigorously optimized based on the nature and volume of the database. In this study, for such optimizations, the grid-search method [70,71] was used. This method involves autonomous, iterative variations in the pair of hyper-parameters – while concurrently employing the 10-fold CV method [69] – to determine optimal values of both hyper-parameters that result in minimum deviation between RF model's predictions and actual observations. The aforesaid deviation between predictions and observations is quantified using all five statistical parameters listed in section 4.2 (i.e., R; R^2; *MAE*; *MAPE*; and *RMSE*). Simply put, hyper-parameters are determined to be optimal when R and R^2 are at (or close to) their global maximum, while *MAE*, *MAPE*, and *RMSE* are at (or close to) their global minimum.

Figs. 3 and 4 show representative (not all) results obtained from the grid-search method. Two of the five statistical parameters (i.e., R and *MAE*) – which were used as measures of deviations of predictions with respect to experimentally-measured values of slump flow and compressive strength – are shown in Figs. 3 and 4. As can be seen, optimal prediction performance of the RF model for both compressive strength and slump flow databases occurred for common values of the two hyper-parameters: that is, *number of trees in the forest* = 500; and *number of splits in each tree* = 9. When the *number of splits* was less than 9, logical splits in the databases were numerically inadequate and too simplistic to fully encompass the complex, underlying correlations between inputs and output. When the *number of splits* was larger than 9, the complex structure of the trees (CARTs) heightened the likelihood of bias, which in turn resulted in overfitting. Likewise, when the *number of trees* was less than 500, the RF model did not have enough independent bootstraps to produce accurate predictions (for new AAC compositions). However, when excessive trees (i.e., >500) were used, while the computational complexity of the model indubitably increased, the prediction performance did not improve (akin to *law of diminishing returns* [66,72]). This is hypothesized to a result of redundancy among the trees. More specifically, it is expected that – in the forest with >500 trees, all of which ought to be distinct – several trees (that were forced to be grown from similar bootstraps) ended up having similar structures, and, therefore, produced similar predictions; as a result, there was little to no improvement in the RF model's overall prediction accuracy. It is worth pointing out that results shown in Figs. 3 and 4 are in good agreement with prior studies that have also reported saturation or decline in prediction performance of RF model when the *number of trees* and/or *number of splits* are increased beyond certain thresholds (depending on the database) to very high values [33,66,67,72]. Lastly, on the bases of results shown in Figs. 3 and 4, in all subsequent applications of the RF model, the *number of trees* and the *number of splits* were fixed at 500 and 9, respectively.

Predictions of compressive strength and slump flow of AACs, as

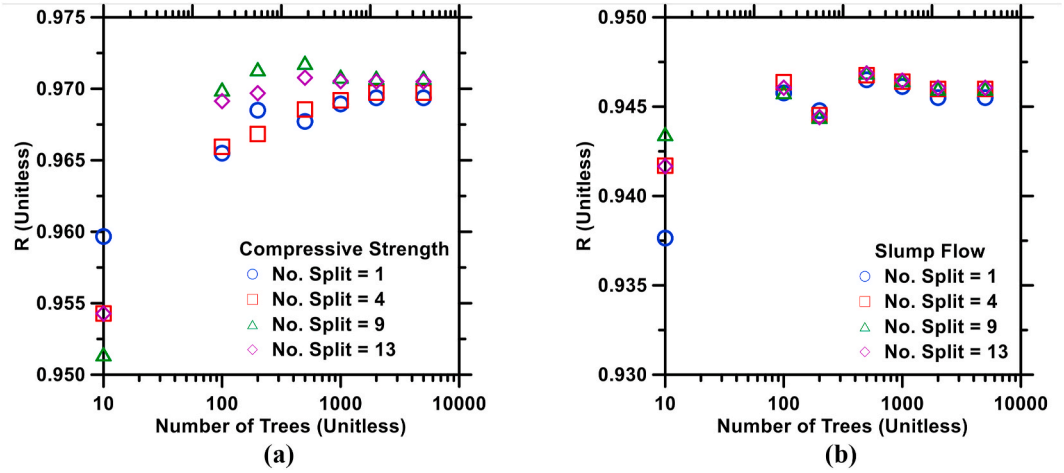

Fig. 3. Grid-search method used to optimize hyper-parameters (*number of trees in the forest*; and *number of splits in each tree*) of the RF model to improve its prediction performance against: **(a)** compressive strength database; and **(b)** slump flow database. The Person correlation coefficient (*R*) is used as a measure of deviation between predictions and observations.

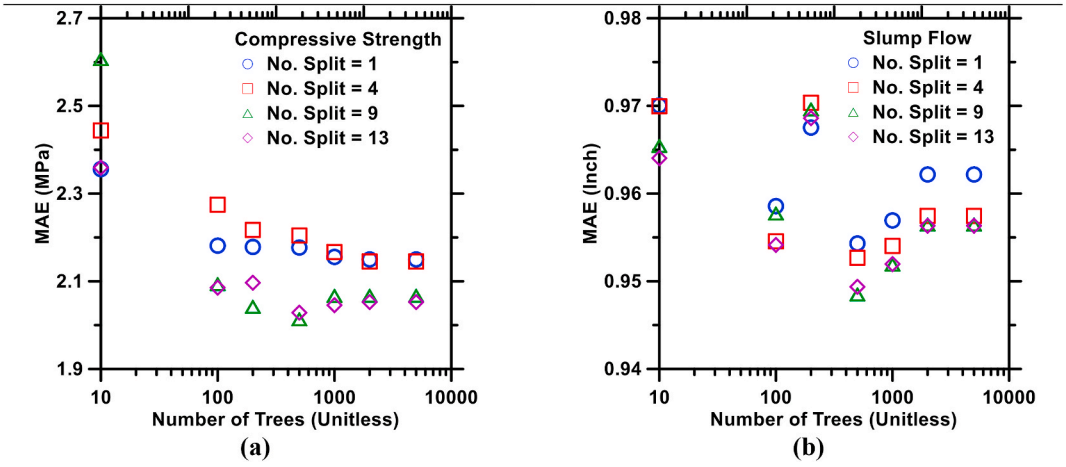

Fig. 4. Grid-search method used to optimize hyper-parameters (*number of trees in the forest*; and *number of splits in each tree*) of the RF model to improve its prediction performance against: **(a)** compressive strength database; and **(b)** slump flow database. The mean absolute error (*MAE*) is used as a measure of deviation between predictions and observations.

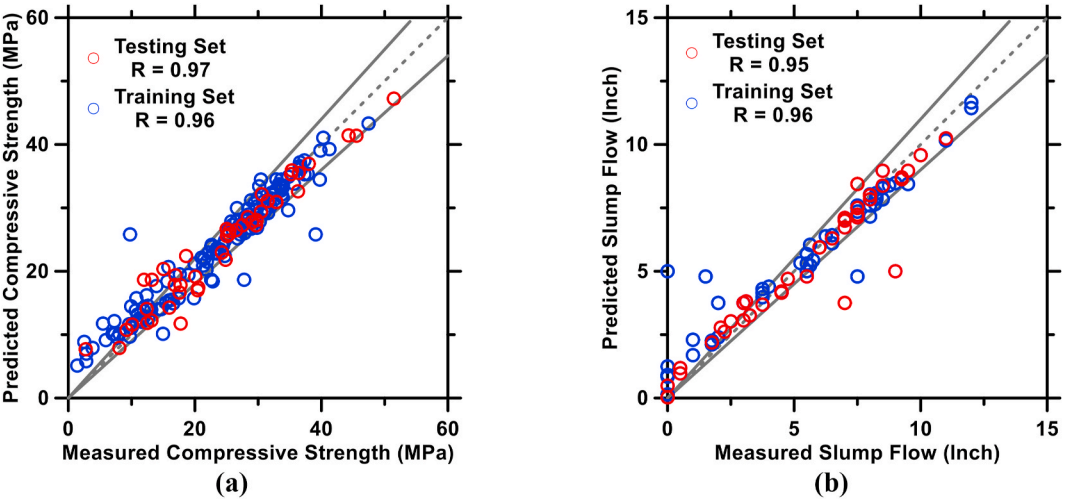

Fig. 5. RF model's predictions of: **(a)** compressive strength; and **(b)** slump flow compared against experimental measurements. Person correlation coefficient (*R*) of the predictions are shown in the legends. The dashed line represents the line of ideality and the solid lines represent a ±10% bound.

produced by the RF model, are shown in Fig. 5. Statistical parameters pertaining to the model's prediction performances are itemized in Table 4. It should be noted that parameters listed in Table 4, collectively, provide quantitative measure of the model's ability (after it is trained) to predict properties of AACs in the testing dataset (N·B.: data-records in the testing set were keep hidden from the model during its training). In Fig. 5, however, RF model's predictions of properties of AACs from the testing set – as well as the training set – are shown. The purpose of including the training set in the figure is to confirm that during training of the model, underfitting and overfitting were minimized. Since *R* of both training and testing sets are similar in Fig. 5, it can indeed be said that underfitting and overfitting was avoided.

As shown in Table 4, the RF model was able to produce accurate predictions of compressive strength of AACs; the root mean squared error (RMSE) was low (≈2 MPa), and the Pearson correlation coefficient (*R*) was high (0.97). Typical standard deviation in experimental measurements of compressive strength of AAC is ≈ 5 MPa [73]. Considering that the mean absolute error (*MAE*) of the RF model's predictions was ≈2 MPa – which is of the same order of magnitude as standard deviation of experimental measurements – it can broadly be said that the RF model can reliably predict compressive strength of AACs. Like predictions of compressive strength, predictions of slump flow were also accurate, albeit slightly inferior compared to compressive strength predictions. The root mean squared error (*RMSE*) of slump flow predictions was 0.95 inches, and the Pearson correlation coefficient (*R*) was 0.95. Accurate predictions of both fresh (slump flow) and hardened (compressive strength) properties of AACs indicate that the methods (i.e., grid-search and 10-fold CV method) used for optimization of the RF model's hyper-parameters were indeed advantageous in developing reliable *composition-properties* correlations without discounting the outliers, and reducing the probabilities of overfitting and underfitting.

Regarding the point made above – that is, RF model's predictions of compressive strength were slightly superior compared to predictions of slump flow (see Table 4 and Fig. 5) – there are two possible explanations. First, it is hypothesized that some physiochemical factors – for example: particle shape of aggregates; mixing speed; etc. – that could potentially influence the slump flow (e.g., small variations in parameters pertaining to the ASTM C143-15 testing procedure that was used) could not be represented in the database. Alternatively, it can be said that if all influential variables were to be exhaustively and accurately accounted for, predictions of slump flow would improve. Second, it is hypothesized that *composition-slump flow* correlations in AACs are inherently more complex than *composition-compressive strength* links. This hypothesis is reasonable considering that slump flow is a property measured at early ages – when multiple, mutually-interacting chemical processes (e.g., dissolution of fly ashes; and precipitation of Al-Si monomers, oligomers, and polymers) either occur simultaneously or in close temporal proximity of one another [13,74,75]. Such dynamic chemical processes occurring within the AAC's microstructure can cause significant time-dependent variations in all early-age properties including slump flow. Furthermore, kinetics of such early-age chemical processes changes rapidly with respect to time [76,77], thus implying that small differences in the time of measurement of early-age properties (e.g., slump flow) could result in significant variability. In contrast, compressive strength, is a mature-state property – measured at > 24 h after mixing – when dissolution-precipitation processes (e.g., nucleation and growth of the reaction product) occurring within the AAC's microstructure are expected to be at dynamic equilibrium and progressing with slow kinetics [76,77]. Due to this, small errors in the time of measurement of compressive strength are expected to result in small – if at all perceptible – error in compressive strength.

Overall, based on the results shown in Table 4 and Fig. 5, it can be said that the RF model is apposite of prediction of properties of AACs. High fidelity predictions of AACs' properties, as produced by the RF model, are not surprising bearing in mind that several past studies have already reported that the RF model produces superior predictions of materials' properties [27–29,33,64] – in general, with only a few exceptions – compared to several other standalone ML models, including the most prevalently-used ones (e.g., artificial neural networks and support vector machines). This disparity in RF model's prediction performance vis-à-vis other ML models can be traced back to the former model's structure which lends several advantages [66,67]. In RF, a large number of trees (i.e., number of CARTs ≫100) are grown, one-by-one in a recursive manner by using randomly-selected bootstraps of identical volume; as such, generalization errors (likelihood of overfitting) are minimized [68]. As each tree is permitted to grow – and not pruned or smoothened at all – until it reaches it maximum size, RF is proficient at developing rational *input-output* correlations, while ensuring that seemingly anomalous data-records (i.e., outliers with respect to already established trends) are not ignored or removed during any stage of the training process. Furthermore, the RF model employs two-stage randomization, which goes a long way in ensuring that each of the *deep unpruned* trees, is distinct in its structure, and does not exhibit any dependency to the rest of the trees in the forest. Such independency among the trees is crucial because it ensures that predictions produced by the trees are truly independent of each other, which in turn results in low variance in the final predictions (i.e., average of predictions from all trees). Lastly, the RF model is easy to implement because the *number of trees in the forest* and *number of splits in each tree* are the only two hyper-parameters that are required as inputs from the user. Adjusting these parameters through trial-and-error is generally cumbersome and time-consuming, and could compromise prediction performance [69]. Therefore, in this study, we used to the grid-search method along with the 10-fold CV method (see Figs. 3 and 4) for such adjustments. Indeed, in our previous study [27], we have shown that such union of RF and an optimization algorithm produces a truly parameter-free model that can predict outputs with high accuracy even in highly complex data-domains (produced by using combination of trigonometric and decaying-exponential functions). In the same study [27], we have shown that artificial neural networks and support vector machines – while generally good at capturing *cause-effect* correlations – fail to accurately predict data points at (and around) the peaks and troughs of such highly complex data-domains.

On the closing note of this section, it is worth emphasizing that the ability of the RF model to produce high-fidelity prediction of AACs' properties makes the model apposite for optimization. Owing the limited volume and diversity of the database that was used in this study, we concede that carrying out all-encompassing optimizations is not feasible. Nevertheless, to demonstrate the *proof-of-concept*, we attempted to capitalize on the excellent prediction performance of the RF model so as to optimize the mixture design of AAC to achieve an imposed (i.e., target) 7-day strength. Two scenarios were considered: (1) the Na_2O content was varied, in step-wise manner, from 25-to-45 kg. m^{-3}; and (2) the CaO content was varied, in step-wise manner, from 90-to-130 kg. m^{-3}. In both scenarios, the remaining input parameters were fixed, and three different target 7-day compressive strengths (i.e., 20 MPa; 25 MPa; and 30 MPa) were imposed as inputs. All input parameters are enumerated in Table 5. Next, the RF model was used to perform "inverse" predictions (as per the Bayesian optimization approach [28]) to reveal optimal values of water content (as output, in relation to the variable Na_2O or CaO content and other fixed input parameters) of AACs

Table 4
Five statistical parameters (i.e., *R, R^2, MAE, MAPE,* and *RMSE*) used to quantify accuracy of RF model's predictions of AACs' compressive strength and slump flow.

	R	R^2	MAE	RMSE	MAPE
Compressive strength	*Unitless*	*Unitless*	*MPa*	*MPa*	*%*
	0.972	0.944	2.013	2.650	13.644
Slump Flow	***Unitless***	***Unitless***	*Inch*	*Inch*	***%***
	0.947	0.897	0.897	0.949	19.546

Table 5
Input parameters and target 7-day compressive strength used to optimize the mixture design (i.e., water content in relation to variable Na_2O and CaO content and other fixed inputs) of AACs.

Attribute	Unit	Scenario 1	Scenario 2
Coarse Aggregate	kg. m^{-3}	959	959
Fine Aggregate	kg. m^{-3}	799	799
SiO_2 Content	kg. m^{-3}	190	190
Al_2O_3 Content	kg. m^{-3}	84	84
Fe_2O_3 Content	kg. m^{-3}	22	22
CaO Content	kg. m^{-3}	122	**90-to-130**
MgO Content	kg. m^{-3}	33	33
Na_2O Content	kg. m^{-3}	**25-to-45**	35
K_2O Content	kg. m^{-3}	2.1	2.1
TiO_2 Content	kg. m^{-3}	5.5	5.5
P_2O_5 Content	kg. m^{-3}	3.6	3.6
MnO Content	kg. m^{-3}	0.09	0.09
Loss on Ignition	kg. m^{-3}	2.7	2.7
SSA of Fly ash	m^2. kg^{-1}	2722	2722
Mixing Procedure	Unitless	7	7
Curing Regime	Unitless	1 (ambient)	1 (ambient)
Curing Temperature	°C	23	23
Curing Time	Days	7	7
Testing Age	Days	7	7
Target compressive Strength	**MPa**	**20-to-30**	**20-to-30**
Water Content	**kg/m^3**	**output**	**output**

that would exhibit the target 7-day compressive strength. Results of these optimizations are shown in Fig. 6. The trends that emerge are in excellent agreement with what is known from theory: (1) For any given Na_2O or CaO content, compressive strength increases with decreasing water content. This is expected considering that lower water content ensures greater solid-to-solid phase connectivity within the microstructure, thereby leading to improved load carrying capacity and compressive strength [74,78,79]; (2) Compressive strength increases with increasing alkali content. This is also reasonable considering that elevated Na content in the system facilitates polymerization of the reaction product, thereby leading to improved strength [7,11,14,78]; and (3) For a given target compressive strength, the optimal water content is slightly lower for Ca-rich fly ashes compared to those with lower calcium content. While the reasons for this are not clear, it is hypothesized that fly ashes with lower calcium content – on account of their inferior hydraulic nature – require slightly larger amount of water for the reaction product's polymerization [80]. To be sure, such agreement between theory and results of the optimization is encouraging, and suggests that more wide-ranging optimizations can be performed, provided that a sufficiently large and diverse *composition-properties* database of AACs can be consolidate to train the RF model.

5.2. *Influence of input parameters on AAC's properties*

In section 5.1, it was shown that the RF model can predict the compressive strength and slump flow of ACCs in relation to their composition and relevant process parameters (e.g., mixing procedure; curing conditions; etc.). In this section, the training of the RF model is leveraged to quantitatively determine the influence of each input parameter (e.g., composition; mixing procedure; curing conditions; etc.) on the resultant properties of the AACs. To this end, the decision-tree structure of the RF model – after it is trained, and fully validated against the test set – was analyzed to estimate and rank each attribute's importance in accordance with the magnitude of influence it exerts on the AACs' slump flow and compressive strength. The results obtained from these analyses are shown in Fig. 7.

As shown in Fig. 7a, the mixing procedure and curing conditions exhibit strong influence on the evolution of AAC's compressive strength; further description of these parameters is provided later in this section. Loss on ignition is also reckoned as very influential; presumably because compressive strength could be undermined if the unburned carbon content in the fly ash is high [8]. As would be expected, the age of testing is important; this is because with increasing age, compressive strength increases monotonically. Interestingly, the water content and compositional parameters are estimated to be substantially less important than the mixing procedure, curing conditions, and unburnt carbon content. This is likely due to the limited variation in, and range of, water contents and fly ashes' compositions in the database used in this study – which impart little effect on a mature property like compressive strength that is measured at $\geq$24 h.

Fig. 7b shows the ranking of input parameters in accordance with their influence on the slump flow of the AACs. As can be seen, water content is the most influential variable that affects slump flow. This is expected because water – based on its content in the AAC – can significantly increase or reduce the viscosity of ACCs; thus, resulting in substantial changes in the slump flow. Loss on ignition – like in the case of compressive strength – is shown to be an influential factor for slump flow; which suggests that the amount of unburnt carbon content can affect early-age reactivity of the fly ash, and thus the evolution of AAC's microstructure and rheological behavior. Alkali content is also deemed

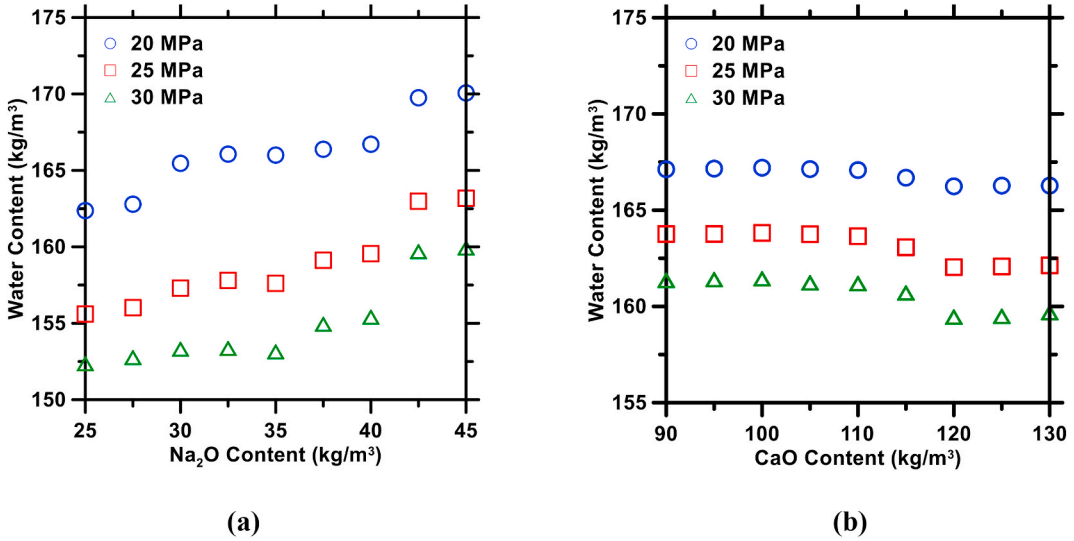

Fig. 6. Optimal value of water content produced by RF model to achieve target compressive strength – of 20 MPa; or 25 MPa; and 30 MPa – in relation to (a) variable Na_2O content; and (b) variable CaO content, while keeping other input parameters relevant to the AACs fixed (shown in Table 5).

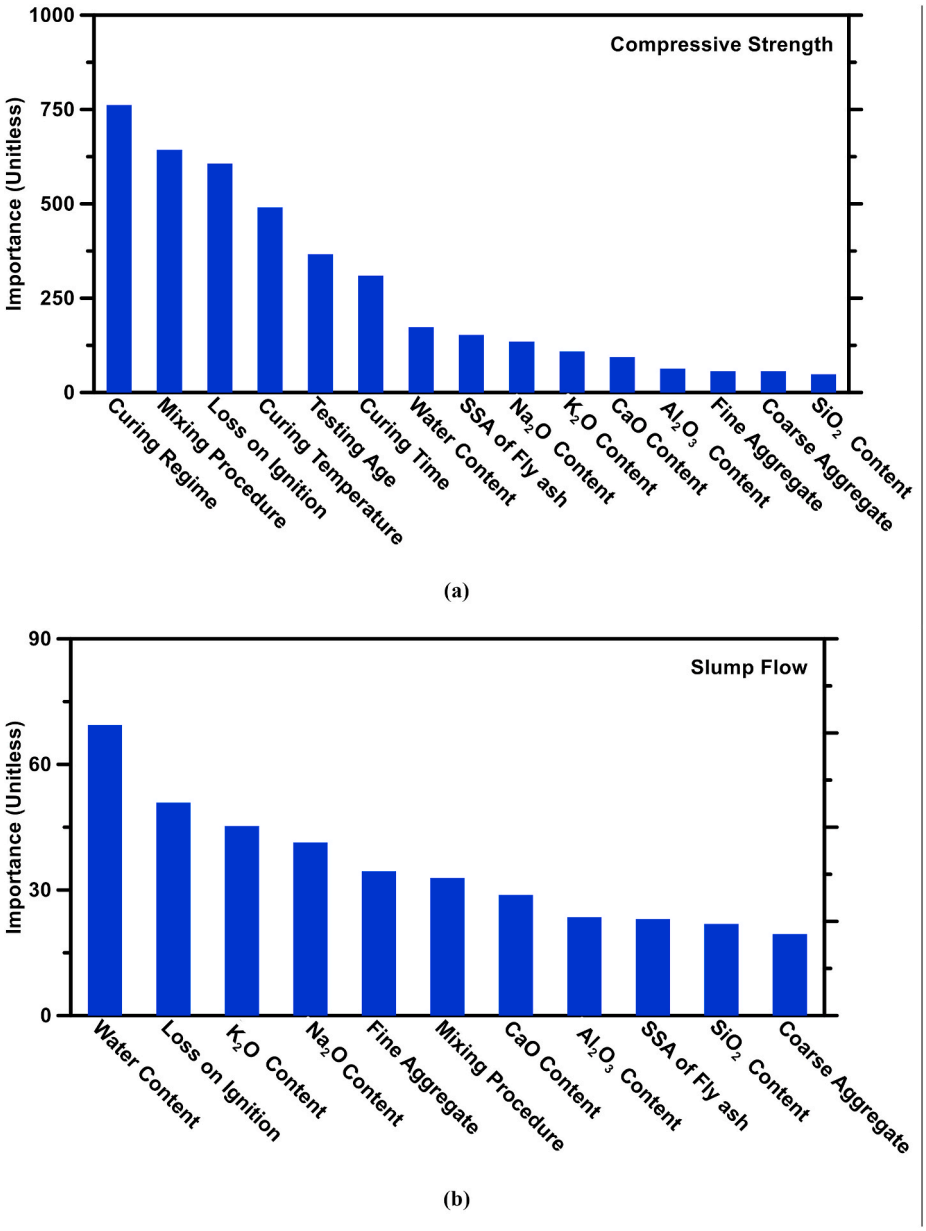

Fig. 7. The importance of input parameters in terms of their contributions towards: **(a)** compressive strength; and **(b)** slump flow of AACs. Parameters are ordered – from left to right – in relation to their decreasing influence on the property.

as important; this is seemingly because of its contribution on the kinetics of precipitation of Al-Si monomers, oligomers, and polymers – all of which dictate the solid-to-solid phase connectivity in the microstructure. In addition to the parameters discussed so far, fine aggregate content (but not coarse aggregate content), mixing procedure, and composition and SSA of fly ash were shown to affect the AACs' slump flow; although to a lesser extent as compared to the influence of water content on AACs' slump flow, and to a greater extent compared to their influence on AACs' compressive strength.

Upon comparing and contrasting the results shown in Fig. 7a and b, it is clear that slump flow – an early-age property – is affected by nearly every input parameter; whereas, compressive strength – a mature property – is largely affected by mixing procedure, curing conditions, and loss on ignition, and less so by other parameters. The mixing procedure – which comprises the sequence of addition of various components of AAC and the mixing duration – exerts significant impact on both the slump flow and compressive strength of the AACs. In this study, it was found that AACs with highest slump flow were those in which water was added prior to adding liquid alkali activators. In these mixtures, water wets and subsequently lubricates the fly ash particulates; thus, reducing the localized concentration of the alkalis when the alkali activator is added. As the local concentration of alkali around a fly ash particulate increases, the dissolution of particulate initiates. If the dissolution of several fly ash particulates is rapid, agglomeration of the mixture in less than a minute becomes likely, which in turn results in poor slump ability. Based on observations from experiments involving different mixing procedures, it was found that gradually adding alkali activators (which accelerates fly ash dissolution in gradual, rather than abrupt, manner), and increasing mixing time – from less than a minute to at least 5 min – benefits not only workability but also compressive strength. The increase in mixing time ensures disaggregation of the floccules and agglomerates that may have formed; which contributes to the improvement of workability [81,82], acceleration of dissolution kinetics of fly ash (due to unlocking of surface area that was diminished due to flocculation and agglomeration) [42], increased rate of precipitation of polymers, enhanced solid-to-solid phase connectivity, and

ultimately reduction of total porosity [41]. Based on results obtained from experiments conducted in this study, mixing procedure 8 was found to be optimal, as it resulted in both superior workability and compressive strength.

Like mixing procedure, curing condition was also determined as an influential parameter for AACs' properties (i.e., compressive strength). Based on our analyses of experimental results, we found – with just a few exceptions – that increasing the curing temperature resulted in improvement of compressive strength and slight reduction in slump flow (results not shown). This, however, is expected because at elevated curing temperatures, the dissolution kinetics of fly ash and precipitation kinetics of the reaction products are enhanced. As a result of these enhancements: the development of the polymeric network (and its solid-to-solid phase connectivity) is faster, which manifests as lower slump flow; and the compressive strength is larger, because of the improved solid-to-solid phase connectivity.

Lastly, alkali and water contents were also determined as influential parameters for AACs' properties – especially the slump flow. In general, low water content aids solid-to-solid phase connectivity in the microstructure, thereby improving load carrying capacity and compressive strength; but resulting in loss of workability [78,79,83]. For a given AAC, the optimal water content depends on the alkali content; wherein AACs with high alkali content require high water content to prevent flash setting and to improve workability. This is because compressive strength is directly proportional to, and slump flow is inversely proportional to, alkali content [48]. The aforesaid correlations are often observed in AACs, because with increasing alkali content, the ensuing enhancement in fly ash dissolution rate facilitates polymerization of the reaction product, thereby leading to lower workability at early ages (i.e., faster development of connected polymeric network) but improved strength at later ages [6,7,14,78]. Based on analyses of the database developed for this study, the optimum alkali-to-fly ash mass ratio was found to be 0.30 [83]. It was found that provision of additional alkali activator (i.e., exceeding the aforesaid ratio of 0.30) resulted in little – if any – improvement in compressive strength.

6. Conclusion

This study presented a random forest (RF) model – a classification-and-regression trees based machine learning (ML) model – to predict two properties of fly ash-based alkali-activated concretes (AACs) that are important from a compliance standpoint: slump flow (a fresh property); and compressive strength (a hardened property). The RF model was used to predict the aforesaid properties as functions of influential parameters pertaining to the AACs: composition of AAC precursors (i.e., fly ash; and alkaline activation solution); curing conditions; and mixing procedures. To the best of the authors' knowledge, this is the first study that employs ML to predict properties of AACs that feature such a wide-range of variations in attributes, including significant disparities in the mixing procedure. This study also places emphasis on leveraging the training of the RF model to quantify the influence of each input parameter on the compressive strength and slump flow of ACCs.

The RF model was rigorously trained using two separate databases: one that mapped physiochemical attributes of >200 different AACs with their slump flow; and one that mapped the same attributes with the concretes' compressive strength. These physiochemical attributes – that were used as inputs within the model – comprised of chemical composition and specific surface areas of six different fly ashes; chemistries of activation solutions prepared using different amounts of NaOH and Na_2SiO_3; different curing temperatures (ranging from 23-to-70 °C); and eight different mixing procedures. The main differences among the mixing procedures used in this study were: (i) the sequence of addition of various components of AAC; and (ii) the duration of mixing at each step of the sequence. During training of the RF model, emphasis was given to rigorously optimize the underlying hyper-parameters – using a combination of grid-search method and 10-fold cross-validation method – so as to: properly establish the inherent inputs-output correlations; account for (as opposed to ignoring or removing) outliers in the database, if any; and keep the variance and bias among trees of the model as low as possible.

Results showed that the RF model – once meticulously trained, and after its intrinsic parameters were rigorously optimized – was able to produce high fidelity predictions (Pearson correlation coefficient, $R \gtrsim 0.95$) of both slump flow and compressive strength of new AACs. Thorough analysis of the RF model's prediction performance was presented in light of prior studies (including ours) that have compared RF model with other prevalent ML models in terms of their abilities to predict properties of heterogeneous material systems and outputs of highly complex (e.g., periodic) functions. Based on such analysis, it was concluded that the RF model's ability to produce accurate predictions of AACs' slump flow and compressive strength can be attributed to two reasons: (1) The structure of the RF model (comprising of deep, unpruned, uncorrelated CARTs) produces an ability to effectively capture the fundamental *cause-effect* relations, even when the database is highly complex; and (2) Implementation of the optimization procedure (i.e., grid-search method used in conjunction with the 10-fold cross-validation method) ensured that the hyper-parameters were tuned and optimized in relation to the nature and volume of the databases.

The RF model was also used to examine the influence of input parameters on the properties of AACs. It was found that mixing procedure and unburnt carbon content exert significant influence on both slump flow and compressive strength. Water content and curing conditions were determined as the most influential input variables for slump flow and compressive strength, respectively. Conversely, SiO_2 content of the fly ash and coarse aggregate content of the AAC were determined as the least influential input variables for both slump flow and compressive strength.

Overall, outcomes of this work show that the RF model – or other RF-based ML models – are apposite ML platforms that could be employed in the future to optimize AAC properties. Of course, for such optimizations to be robust, it is critical that the model be trained with a comprehensive database that not only has a large volume (1000s-to10,000s of unique data-records) but also encompasses tremendous diversity (i.e., substantial variations in chemistries of fly ashes and alkaline activation solutions; curing temperatures; mixing procedures; etc.). Such RF model-based optimization tools could facilitate the materials–by–design approach – which is in alignment with the United States (U.S.) Materials Genome Initiative [84–86] – and expedite the design of AACs with desired properties.

Declaration of competing interest

The authors declare that they have no known competing financial interests or personal relationships that could have appeared to influence the work reported in this paper.

Acknowledgements

Financial support for this research was provided by: the Leonard Wood Institute (LWI: W911NF-07-2-0062); the Federal Highway Administration (Grant: 693JJ31950021); the National Science Foundation (NSF-CMMI: 1661609; and NSF-CMMI: 1932690); the Missouri Department of Transportation (MoDOT); the Missouri Department of Natural Resources (MoDNR); and Ameren Corporation.

Appendix A. Supplementary data

Supplementary data related to this article can be found at https://doi.org/10.1016/j.cemconcomp.2020.103863.

References

[1] C. Shi, A.F. Jiménez, A. Palomo, New cements for the 21st century: the pursuit of an alternative to Portland cement, Cement Concr. Res. 41 (2011) 750–763, https://doi.org/10.1016/j.cemconres.2011.03.016.

[2] J.S. Damtoft, J. Lukasik, D. Herfort, D. Sorrentino, E.M. Gartner, Sustainable development and climate change initiatives, Cement Concr. Res. 38 (2008) 115–127, https://doi.org/10.1016/j.cemconres.2007.09.008.

[3] E. Gartner, H. Hirao, A review of alternative approaches to the reduction of CO_2 emissions associated with the manufacture of the binder phase in concrete, Cement Concr. Res. 78 (Part A) (2015) 126–142, https://doi.org/10.1016/j.cemconres.2015.04.012.

[4] Bridge Replacement Unit Costs 2017 - Bridge Tables - National Bridge Inventory - Bridge Inspection - Safety - Bridges & Structures - Federal Highway Administration. https://www.fhwa.dot.gov/bridge/nbi/sd2017.cfm (accessed March 14, 2019).

[5] Failure to Act Report, ASCE's 2017 Infrastructure Report Card. https://www.infrastructurereportcard.org/the-impact/failure-to-act-report/ (accessed March 14, 2019), report.

[6] J. Davidovits, Geopolymer Chemistry and Applications, fourth ed., Institut Geopolymere, 2015.

[7] J.L. Provis, S.A. Bernal, Geopolymers and related alkali-activated materials, Annu. Rev. Mater. Res. 44 (2014) 299–327, https://doi.org/10.1146/annurev-matsci-070813-113515.

[8] T. Luukkonen, Z. Abdollahnejad, J. Yliniemi, P. Kinnunen, M. Illikainen, One-part alkali-activated materials: a review, Cement Concr. Res. 103 (2018) 21–34, https://doi.org/10.1016/j.cemconres.2017.10.001.

[9] F. Pacheco-Torgal, J. Castro-Gomes, S. Jalali, Alkali-activated binders: a review: Part 1. historical background, terminology, reaction mechanisms and hydration products, Construct. Build. Mater. 22 (2008) 1305–1314, https://doi.org/10.1016/j.conbuildmat.2007.10.015.

[10] J.L. Provis, A. Palomo, C. Shi, Advances in understanding alkali-activated materials, Cement Concr. Res. 78 (Part A) (2015) 110–125, https://doi.org/10.1016/j.cemconres.2015.04.013.

[11] J. Davidovits, Geopolymers and geopolymeric materials, J. Therm. Anal. 35 (1989) 429–441, https://doi.org/10.1007/BF01904446.

[12] J. Davidovits, Geopolymers, Journal of Thermal Analysis 37 (1991) 1633–1656, https://doi.org/10.1007/BF01912193.

[13] P. Duxson, A. Fernández-Jiménez, J.L. Provis, G.C. Lukey, A. Palomo, J.S.J. Van Deventer, Geopolymer technology: the current state of the art, J. Mater. Sci. 42 (2007) 2917–2933, https://doi.org/10.1007/s10853-006-0637-z.

[14] P. Duxson, J.L. Provis, Designing precursors for geopolymer cements, J. Am. Ceram. Soc. 91 (2008) 3864–3869, https://doi.org/10.1111/j.1551-2916.2008.02787.x.

[15] S.A. Bernal, J.L. Provis, Durability of alkali-activated materials: progress and perspectives, J. Am. Ceram. Soc. 97 (2014) 997–1008, https://doi.org/10.1111/jace.12831.

[16] Z. Zhang, J.L. Provis, J. Zou, A. Reid, H. Wang, Toward an indexing approach to evaluate fly ashes for geopolymer manufacture, Cement Concr. Res. 85 (2016) 163–173, https://doi.org/10.1016/j.cemconres.2016.04.007.

[17] K.L. Aughenbaugh, T. Williamson, M.C.G. Juenger, Critical evaluation of strength prediction methods for alkali-activated fly ash, Mater. Struct. 48 (2015) 607–620, https://doi.org/10.1617/s11527-014-0496-z.

[18] Z. Zhang, J.L. Provis, A. Reid, H. Wang, Fly ash-based geopolymers: the relationship between composition, pore structure and efflorescence, Cement Concr. Res. 64 (2014) 30–41, https://doi.org/10.1016/j.cemconres.2014.06.004.

[19] M.C.G. Juenger, R. Siddique, Recent advances in understanding the role of supplementary cementitious materials in concrete, Cement Concr. Res. 78 (Part A) (2015) 71–80, https://doi.org/10.1016/j.cemconres.2015.03.018.

[20] M.C.G. Juenger, R. Snellings, S.A. Bernal, Supplementary cementitious materials: new sources, characterization, and performance insights, Cement Concr. Res. 122 (2019) 257–273, https://doi.org/10.1016/j.cemconres.2019.05.008.

[21] ASTM, C618-15, Specification for Coal Fly Ash and Raw or Calcined Natural Pozzolan for Use in Concrete, ASTM International, 2019, https://doi.org/10.1520/C0618-15.

[22] W.K.W. Lee, J.S.J. van Deventer, Structural reorganisation of class F fly ash in alkaline silicate solutions, Colloid. Surface. Physicochem. Eng. Aspect. 211 (2002) 49–66, https://doi.org/10.1016/S0927-7757(02)00237-6.

[23] T. Bakharev, Durability of geopolymer materials in sodium and magnesium sulfate solutions, Cement Concr. Res. 35 (2005) 1233–1246, https://doi.org/10.1016/j.cemconres.2004.09.002.

[24] T. Bakharev, Geopolymeric materials prepared using Class F fly ash and elevated temperature curing, Cement Concr. Res. 35 (2005) 1224–1232, https://doi.org/10.1016/j.cemconres.2004.06.031.

[25] B. Singh, G. Ishwarya, M. Gupta, S.K. Bhattacharyya, Geopolymer concrete: a review of some recent developments, Construct. Build. Mater. 85 (2015) 78–90, https://doi.org/10.1016/j.conbuildmat.2015.03.036.

[26] D. Dao, S. Trinh, H.-B. Ly, B. Pham, Prediction of compressive strength of geopolymer concrete using entirely steel slag aggregates: novel hybrid artificial intelligence approaches, Appl. Sci. 9 (2019) 1113, https://doi.org/10.3390/app9061113.

[27] R. Cook, J. Lapeyre, H. Ma, A. Kumar, Prediction of compressive strength of concrete: a critical comparison of performance of a hybrid machine learning model with standalone models, ASCE Journal of Materials in Civil Engineering 31 (2019), 04019255, https://doi.org/10.1061/(ASCE)MT.1943-5533.0002902.

[28] T. Han, A. Siddique, K. Khayat, J. Huang, A. Kumar, An ensemble machine learning approach for prediction and optimization of modulus of elasticity of recycled aggregate concrete, Construct. Build. Mater. 244 (2020) 118271, https://doi.org/10.1016/j.conbuildmat.2020.118271.

[29] J.-S. Chou, C.-F. Tsai, A.-D. Pham, Y.-H. Lu, Machine learning in concrete strength simulations: multi-nation data analytics, Construct. Build. Mater. 73 (2014) 771–780, https://doi.org/10.1016/j.conbuildmat.2014.09.054.

[30] A. Behnood, V. Behnood, M.M. Gharehveran, K.E. Alyamac, Prediction of the compressive strength of normal and high-performance concretes using M5P model tree algorithm, Construct. Build. Mater. 142 (2017) 199–207, https://doi.org/10.1016/j.conbuildmat.2017.03.061.

[31] J.-S. Chou, C.-K. Chiu, M. Farfoura, I. Al-Taharwa, Optimizing the prediction accuracy of concrete compressive strength based on a comparison of data-mining techniques, J. Comput. Civ. Eng. 25 (2010) 242–253, https://doi.org/10.1061/(ASCE)CP.1943-5487.0000088.

[32] Z.H. Duan, S.C. Kou, C.S. Poon, Using artificial neural networks for predicting the elastic modulus of recycled aggregate concrete, Construct. Build. Mater. 44 (2013) 524–532, https://doi.org/10.1016/j.conbuildmat.2013.02.064.

[33] T. Han, N. Stone-Weiss, J. Huang, A. Goel, A. Kumar, Machine learning as a tool to design glasses with controlled dissolution for application in healthcare industry, Acta Biomater. 107 (2020) 286–298, https://doi.org/10.1016/j.actbio.2020.02.037.

[34] D. Dao, H.-B. Ly, S. Trinh, T.-T. Le, B. Pham, Artificial intelligence approaches for prediction of compressive strength of geopolymer concrete, Materials 12 (2019) 983, https://doi.org/10.3390/ma12060983.

[35] M. Lahoti, P. Narang, K.H. Tan, E.-H. Yang, Mix design factors and strength prediction of metakaolin-based geopolymer, Ceram. Int. 43 (2017) 11433–11441, https://doi.org/10.1016/j.ceramint.2017.06.006.

[36] K.T. Nguyen, Q.D. Nguyen, T.A. Le, J. Shin, K. Lee, Analyzing the compressive strength of green fly ash based geopolymer concrete using experiment and machine learning approaches, Construct. Build. Mater. 247 (2020) 118581, https://doi.org/10.1016/j.conbuildmat.2020.118581.

[37] P.R. Prem, A. Thirumalaiselvi, M. Verma, Applied linear and nonlinear statistical models for evaluating strength of Geopolymer concrete, Comput. Concr. 24 (2019) 7–17, https://doi.org/10.12989/CAC.2019.24.1.007.

[38] N.K. Lee, H.K. Lee, Setting and mechanical properties of alkali-activated fly ash/slag concrete manufactured at room temperature, Construct. Build. Mater. 47 (2013) 1201–1209, https://doi.org/10.1016/j.conbuildmat.2013.05.107.

[39] P.S. Deb, P. Nath, P.K. Sarker, The effects of ground granulated blast-furnace slag blending with fly ash and activator content on the workability and strength properties of geopolymer concrete cured at ambient temperature 62, Materials & Design, 1980-2015, pp. 32–39, https://doi.org/10.1016/j.matdes.2014.05.001, 2014.

[40] A. Muthadhi, V. Dhivya, Investigating strength properties of geopolymer concrete with quarry dust, ACI Mater. J. 114 (2017), https://doi.org/10.14359/51689674.

[41] M. Palacios, F. Puertas, Effectiveness of mixing time on hardened properties of waterglass-activated slag pastes and mortars, ACI Mater. J. 108 (2011) 73–78.

[42] P. Chindaprasirt, P. De Silva, S. Hanjitsuwan, Effect of high-speed mixing on properties of high calcium fly ash geopolymer paste, Arabian J. Sci. Eng. 39 (2014) 6001–6007, https://doi.org/10.1007/s13369-014-1217-1.

[43] B.A. Young, A. Hall, L. Pilon, P. Gupta, G. Sant, Can the compressive strength of concrete be estimated from knowledge of the mixture proportions?: new insights from statistical analysis and machine learning methods, Cement Concr. Res. 115 (2019) 379–388, https://doi.org/10.1016/j.cemconres.2018.09.006.

[44] L.H. Gilpin, D. Bau, B.Z. Yuan, A. Bajwa, M. Specter, L. Kagal, Explaining explanations: an overview of interpretability of machine learning, 2018, in: IEEE 5th International Conference on Data Science and Advanced Analytics (DSAA), IEEE, Turin, Italy, 2018, pp. 80–89, https://doi.org/10.1109/DSAA.2018.00018.

[45] D05 Committee, D4326-13 Standard Test Method for Major and Minor Elements in Coal and Coke Ash by X-Ray Fluorescence, ASTM International, West Conshohocken, PA, 2013, https://doi.org/10.1520/D4326-13.

[46] C09 Committee, C618-19 Standard Specification for Coal Fly Ash and Raw or Calcined Natural Pozzolan for Use in Concrete, ASTM International, West Conshohocken, PA, 2019, https://doi.org/10.1520/C0618-19.

[47] I. Odler, The BET-specific surface area of hydrated Portland cement and related materials, Cement Concr. Res. 33 (2003), https://doi.org/10.1016/S0008-8846(03)00225-4, 2049–2056.

[48] E. Gomaa, S. Sargon, C. Kashosi, M. ElGawady, Fresh properties and compressive strength of high calcium alkali activated fly ash mortar, Journal of King Saud University - Engineering Sciences 29 (2017) 356–364, https://doi.org/10.1016/j.jksues.2017.06.001.

[49] P. Chindaprasirt, T. Chareerat, V. Sirivivatnanon, Workability and strength of coarse high calcium fly ash geopolymer, Cement Concr. Compos. 29 (2007) 224–229, https://doi.org/10.1016/j.cemconcomp.2006.11.002.

[50] H. Cho, A.R. Felmy, R. Craciun, J.P. Keenum, N. Shah, D.A. Dixon, Solution state structure determination of silicate oligomers by ^{29} Si NMR spectroscopy and molecular modeling, J. Am. Chem. Soc. 128 (2006) 2324–2335, https://doi.org/10.1021/ja0559202.

[51] P. Chindaprasirt, P. De Silva, K. Sagoe-Crentsil, S. Hanjitsuwan, Effect of SiO2 and Al2O3 on the setting and hardening of high calcium fly ash-based geopolymer systems, J. Mater. Sci. 47 (2012) 4876–4883, https://doi.org/10.1007/s10853-012-6353-y.

[52] M.S. Morsy, S.H. Alsayed, Y. Al-Salloum, T. Almusallam, Effect of sodium silicate to sodium hydroxide ratios on strength and microstructure of fly ash geopolymer binder, Arabian J. Sci. Eng. 39 (2014) 4333–4339, https://doi.org/10.1007/s13369-014-1093-8.

[53] W.K. Part, M. Ramli, C.B. Cheah, An overview on the influence of various factors on the properties of geopolymer concrete derived from industrial by-products,

Construct. Build. Mater. 77 (2015) 370–395, https://doi.org/10.1016/j.conbuildmat.2014.12.065.
[54] P. Topark-Ngarm, P. Chindaprasirt, V. Sata, Setting time, strength, and bond of high-calcium fly ash geopolymer concrete, J. Mater. Civ. Eng. 27 (2015), 04014198, https://doi.org/10.1061/(ASCE)MT.1943-5533.0001157.
[55] C09 Committee, C127-15 Standard Test Method Test Method for Relative Density (Specific Gravity) and Absorption of Coarse Aggregate, ASTM International, West Conshohocken, PA, 2015, https://doi.org/10.1520/C0127-15.
[56] C09 Committee, C33/C33M-16 Standard Specification for Concrete Aggregates, ASTM International, West Conshohocken, PA, 2016, https://doi.org/10.1520/C0033_C0033M-16.
[57] M.A. Taylor, Concrete mix proportioning by modified fineness modulus method, Concr. Int. 8 (1986) 47–52.
[58] C09 Committee, C143/C143M-15a Standard Test Method for Slump of Hydraulic-Cement Concrete, ASTM International, 2015, https://doi.org/10.1520/C0143_C0143M-15A.
[59] C09 Committee, C192/C192M-16 Standard Practice for Making and Curing Concrete Test Specimens in the Laboratory, ASTM International, 2016, https://doi.org/10.1520/C0192_C0192M-16.
[60] C09 Committee, C39/C39M-16 Standard Test Method for Compressive Strength of Cylindrical Concrete Specimens, ASTM International, 2016, https://doi.org/10.1520/C0039_C0039M-16.
[61] D. Jansen, F. Goetz-Neunhoeffer, C. Stabler, J. Neubauer, A remastered external standard method applied to the quantification of early OPC hydration, Cement Concr. Res. 41 (2011) 602–608, https://doi.org/10.1016/j.cemconres.2011.03.004.
[62] G. Le Saoût, B. Lothenbach, A. Hori, T. Higuchi, F. Winnefeld, Hydration of Portland cement with additions of calcium sulfoaluminates, Cement Concr. Res. 43 (2013) 81–94, https://doi.org/10.1016/j.cemconres.2012.10.011.
[63] G. Le Saoût, V. Kocaba, K. Scrivener, Application of the Rietveld method to the analysis of anhydrous cement, Cement Concr. Res. 41 (2011) 133–148, https://doi.org/10.1016/j.cemconres.2010.10.003.
[64] R. Cook, C.M. Keitumetse, M.B. Hayat, A. Kumar, L. Alagha, Prediction of Flotation Performance of Sulfide Minerals Using an Original Hybrid Machine Learning Model, Engineering Reports, Article in Press, 2020, pp. 1–33, https://doi.org/10.1002/eng2.12167.
[65] L. Breiman, Bagging predictors, Mach. Learn. 24 (1996) 123–140, https://doi.org/10.1007/BF00058655.
[66] L. Breiman, Random forests, Mach. Learn. 45 (2001) 5–32.
[67] X. Chen, H. Ishwaran, Random forests for genomic data analysis, Genomics 99 (2012) 323–329.
[68] Găš Biau, L. Devroye, Găą Lugosi, Consistency of random forests and other averaging classifiers, J. Mach. Learn. Res. 9 (2008) 2015–2033.
[69] C. Schaffer, Selecting a classification method by cross-validation, Mach. Learn. 13 (1993) 135–143, https://doi.org/10.1007/BF00993106.
[70] T. Eitrich, B. Lang, Efficient optimization of support vector machine learning parameters for unbalanced datasets, J. Comput. Appl. Math. 196 (2006) 425–436, https://doi.org/10.1016/j.cam.2005.09.009.
[71] J. Bergstra, Y. Bengio, Random search for hyper-parameter optimization, J. Mach. Learn. Res. 13 (2012) 281–305.
[72] M.R. Segal, Machine Learning Benchmarks and Random Forest Regression, 2004. https://escholarship.org/uc/item/35x3v9t4. (Accessed 18 April 2020).
[73] E. Nawy (Ed.), Concrete Construction Engineering Handbook, CRC Press, 2008, https://doi.org/10.1201/9781420007657.
[74] J.L. Provis, J.S.J. Van Deventer, Geopolymers: Structures, Processing, Properties and Industrial Applications, Elsevier, 2009.
[75] T. Oey, A. Kumar, I. Pignatelli, Y. Yu, N. Neithalath, J.W. Bullard, M. Bauchy, G. Sant, Topological controls on the dissolution kinetics of glassy aluminosilicates, J. Am. Ceram. Soc. 100 (2017) 5521–5527, https://doi.org/10.1111/jace.15122.
[76] S. De, K. Sagoe-Crentsil, V. Sirivivatnanon, Kinetics of geopolymerization: role of Al_2O_3 and SiO_2, Cement Concr. Res. 37 (2007) 512–518, https://doi.org/10.1016/j.cemconres.2007.01.003.
[77] J.L. Provis, J.S.J. Van Deventer, Geopolymerisation kinetics. 2. Reaction kinetic modelling, Chem. Eng. Sci. 62 (2007) 2318–2329, https://doi.org/10.1016/j.ces.2007.01.028.
[78] P. Duxson, J.L. Provis, G.C. Lukey, S.W. Mallicoat, W.M. Kriven, J.S. Van Deventer, Understanding the relationship between geopolymer composition, microstructure and mechanical properties, Colloid. Surface. Physicochem. Eng. Aspect. 269 (2005) 47–58, https://doi.org/10.1016/j.colsurfa.2005.06.060.
[79] J.G.S. van Jaarsveld, J.S.J. van Deventer, G.C. Lukey, The effect of composition and temperature on the properties of fly ash- and kaolinite-based geopolymers, Chem. Eng. J. 89 (2002) 63–73, https://doi.org/10.1016/S1385-8947(02)00025-6.
[80] P. Chindaprasirt, T. Phoo-ngernkham, S. Hanjitsuwan, S. Horpibulsuk, A. Poowancum, B. Injorhor, Effect of calcium-rich compounds on setting time and strength development of alkali-activated fly ash cured at ambient temperature, Case Studies in Construction Materials 9 (2018), e00198, https://doi.org/10.1016/j.cscm.2018.e00198.
[81] M. Palacios, P.F.G. Banfill, F. Puertas, Rheology and setting of alkali-activated slag pastes and mortars: effect if organic admixture, ACI Mater. J. 105 (2008) 140–148.
[82] F. Puertas, B. González-Fonteboa, I. González-Taboada, M.M. Alonso, M. Torres-Carrasco, G. Rojo, F. Martínez-Abella, Alkali-activated slag concrete: fresh and hardened behaviour, Cement Concr. Compos. 85 (2018) 22–31, https://doi.org/10.1016/j.cemconcomp.2017.10.003.
[83] J.L. Provis, J.S.J. Van Deventer, 1 - introduction to geopolymers, in: J.L. Provis, J.S.J. van Deventer (Eds.), Geopolymers, Woodhead Publishing, 2009, pp. 1–11, https://doi.org/10.1533/9781845696382.1.
[84] J.J. de Pablo, N.E. Jackson, M.A. Webb, L.-Q. Chen, J.E. Moore, D. Morgan, R. Jacobs, T. Pollock, D.G. Schlom, E.S. Toberer, J. Analytis, I. Dabo, D. M. DeLongchamp, G.A. Fiete, G.M. Grason, G. Hautier, Y. Mo, K. Rajan, E.J. Reed, E. Rodriguez, V. Stevanovic, J. Suntivich, K. Thornton, J.-C. Zhao, New frontiers for the materials genome initiative, Npj Computational Materials 5 (2019) 41, https://doi.org/10.1038/s41524-019-0173-4.
[85] M.L. Green, J. Hattrick-Simpers, G. Kusne, Z. Trautt, The materials genome initiative revolution, SAMPE J. 55 (2019) 6–13.
[86] J.A. Warren, The materials genome initiative and artificial intelligence, MRS Bull. 43 (2018) 452–457, https://doi.org/10.1557/mrs.2018.122.